Available online at www.sciencedirect.com
SCIENCE DIRECT®
ELSEVIER
International Journal of Solids and Structures 43 (2006) 4465–4483
INTERNATIONAL JOURNAL OF SOLIDS and STRUCTURES
www.elsevier.com/locate/ijsolstr

Ductility of interstitial-free steel under high strain rate tension: Experiments and macroscopic modeling with a physically-based consideration

M. Kuroda [a,*], A. Uenishi [b], H. Yoshida [b], A. Igarashi [a,1]

[a] *Department of Mechanical Systems Engineering, Yamagata University, Jonan 4-3-16, Yonezawa, Yamagata 992-8510, Japan*
[b] *Forming Technologies R&D Center, Steel Research Laboratories, Nippon Steel Corporation, Shintomi 20-1, Futtsu, Chiba 293-8511, Japan*

Received 9 March 2005; received in revised form 21 June 2005
Available online 24 August 2005

Abstract

In this paper, an experimental investigation and a constitutive modeling of the mechanical response of an interstitial-free (IF) steel over a wide range of strain rates (from 0.001/s to 750/s) are presented. Tensile tests at relatively high strain rates, exceeding 100/s, are performed at an initial room temperature, using the so-called one bar technique developed on the basis of the Hopkinson bar method. At a high strain rate, a distinct upper yield limit is observed, and the subsequent flow stress increases remarkably. Furthermore, the ductility is reduced significantly in comparison to the case of low strain rate tension. In order to express such a complicated material response of IF steel, we develop a new constitutive model that takes into account effects of a change in the mobile dislocation density and thermal softening. The model can be easily applicable to large-scale engineering computations, because it is macroscopically formulated. We try to reproduce the tensile response including a diffuse neck formation at high strain rates, using the proposed constitutive model and finite element method. The results indicate that a change in the mobile dislocation density, together with thermal softening, has substantial effects on apparent work hardening behavior at high strain rates, although the change in the mobile dislocation density is transcribed at macroscopic scale in the model. Finally, we discuss characteristics of true stress–true strain curves at various strain rates, and their correlation with the plastic instability behavior.

Keywords: Strain rate; Ductility; Elastic–viscoplastic material; Finite strain; Mechanical testing

* Corresponding author. Tel.: +81 238 26 3211; fax: +81 238 26 3205.
E-mail address: kuroda@yz.yamagata-u.ac.jp (M. Kuroda).
[1] Present address: Nissan Shatai Co., LTD., Hiratsuka, Kanagawa 254-0012, Japan.

0020-7683/$ - see front matter © 2005 Elsevier Ltd. All rights reserved.
doi:10.1016/j.ijsolstr.2005.06.076

1. Introduction

Interstitial-free (IF) steel generally has low yield strength, high Lankford's *r*-value, high strain rate sensitivity and good formability. IF steel is widely used as a base material to develop high-strength steels with addition of Mn, Si, P, etc.

It is known that the ductility of IF steel under uniaxial tensile tests decreases with increase of imposed strain rate, exhibiting a very large upper yield limit at a high strain rate (Uenishi and Teodosiu, 2003; also see Fig. 3 in the next section). Almost the same tendency was observed for pure irons, and the reduction of the ductility at a high strain rate was referred to as *high-velocity brittleness* in Kawata et al. (1985). Such complicated material behaviors under high strain rate tensile tests have not been fully investigated so far.

In this paper, first, an experimental investigation of the mechanical response of an IF steel sheet over a wide range of strain rates from 0.001/s to 750/s is carried out. Tensile tests at relatively high strain rates, exceeding 100/s, are performed at an initial room temperature, using the so-called one bar technique developed on the basis of the Hopkinson bar method (Kawata et al., 1979; Itabashi, 2003). Thermal softening behavior of the material is also investigated. Secondly, in order to express the complicated material response, we develop a new constitutive model that takes into account effects of a change in the mobile dislocation density and thermal softening. The model can be easily applicable to large-scale engineering computations, because it is macroscopically formulated. We try to reproduce the tensile response including a diffuse neck formation at high strain rates, using the proposed constitutive model and finite element method. The results indicate that a change in the mobile dislocation density, together with thermal softening, has substantial effects on apparent work hardening behavior at high strain rates, although the change in the mobile dislocation density is transcribed at macroscopic scale in the model. It is shown that the proposed model has a sufficient capability to reproduce the complicated material response over a wide range of strain rates. Finally, we discuss characteristics of true stress–true strain curves at various strain rates, and their correlation with the plastic instability behavior.

2. Experiments

The material used is a commercial IF steel sheet with 1.2 mm thick (mass %: 0.001 C, 0.08 Mn, 0.052 Ti, 0.032 Al, 0.004 Si, 0.012 P, 0.007 S), which was hot and cold-rolled and was subsequently subjected to recrystallization and annealing. Fig. 1 shows the optical micrograph of an undeformed sample. The average grain size in this figure is about 20 μm.

Mechanical tensile tests at different nominal strain rates from 0.001/s to 750/s were carried out at room temperature. The tensile tests at nominal strain rates higher than 100/s were conducted using a one bar type of Hopkinson method, referred to henceforth simply as *one bar method* (Kawata et al., 1979; Itabashi, 2003), whereas an Instron-type testing machine was employed for the tests at nominal strain rates lower than about 1/s. A schematic illustration of the one bar method and the specimen shapes are shown in Fig. 2.

In the original Hopkinson bar method, the specimen is placed between two long, uniform, cylindrical bars. One of the bars (the incident bar) is used to give a stress pulse, which is generated in some cases by a striker tube, and the other (transmitter bar) is used to measure the stress in the specimen, which is proportional to the amplitude of the transmitted wave. The duration of the stress pulse limits maximum strain of the specimen at a given strain rate, and thus it is not always simple to carry out experiments for ductile materials. An impact block, instead of the incident bar, features the one bar method. As shown in Fig. 2(a), the testing system of the one bar method consists of an impact block, a hammer, an output bar and a specimen. When the hammer gives an impact to the impact block, the specimen is deformed in tension. Simultaneously, the elastic wave starts to propagate in the output bar. A strain value $\varepsilon_g(t)$ of the output bar is measured at a distance a from the end of the output bar, where t is the natural time, In addition,

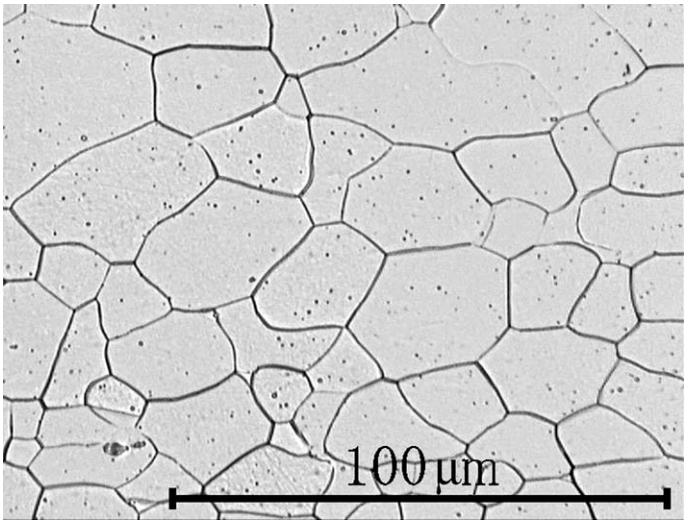

Fig. 1. Optical micrograph of IF steel sheet material.

an electro-optical displacement transducer is used to measure the velocity $V(t)$ of the impact block. Using one-dimensional elastic wave theory, the nominal strain $\varepsilon_N(t)$ and nominal stress $\sigma_N(t)$ of the specimen are calculated as follows (Kawata et al., 1979):

$$\varepsilon_N(t) = \frac{1}{L_s}\int_0^t \left[V(\xi) - c\varepsilon_g\left(\xi + \frac{a}{c}\right)\right] d\xi, \tag{1}$$

$$\sigma_N(t) = \frac{A_o E_o \varepsilon_g(t + a/c)}{A_s}, \tag{2}$$

where L_s and A_s are the gage length and cross-sectional area of the specimen, and A_o, E_o and c are the cross-sectional area, Young's modulus and longitudinal elastic wave velocity of the output bar, respectively. The derivative of $\varepsilon_N(t)$ with respect to the time t gives a nominal strain rate. The one bar method can fundamentally extract a feature of the material response without apparent vibration effects that are usually seen for a short load cell causing multiple passage of reflected longitudinal elastic waves. The one bar equipment employed here has been further improved by adding attachments for preventing initial lateral vibrations of the output bar, which causes a pseudo-initial stress peak at a yield point (Yoshida, 2001; Uenishi et al., 2003). As a consequence, an experimental result obtained with this improved equipment can be regarded as a plain material response free from any apparent vibration effect. All the specimens were made so that the tensile axis coincides with the rolling direction (RD).

Fig. 3 shows nominal stress–nominal strain curves at several strain rates. The nominal stress is given by dividing the tensile load by the initial cross-sectional area of the parallel gage region (the nominal stress is given by Eq. (2) for the one bar tests). The nominal strain is obtained by dividing the elongation by the corresponding reference gage length (the nominal strain is given by Eq. (1) for the one bar tests). The reference gage length is chosen to be 10 mm ($= L_s$) for the one bar tests as shown in Fig. 2(b), while it is taken to be 8 mm for the low strain rate tests ($\leqslant 1/s$) following the length of the extensometer used. In a strict sense, the overall nominal stress–nominal strain curves for the high and low strain rates cannot be compared directly because of the difference of the reference gage lengths. But, it is clearly seen that the ductility of the specimen is much greater at the low strain rates than at the high strain rates. Fig. 4 shows photographs of the specimens after testing. It is seen from Fig. 3 that the profiles of the nominal stress–nominal strain

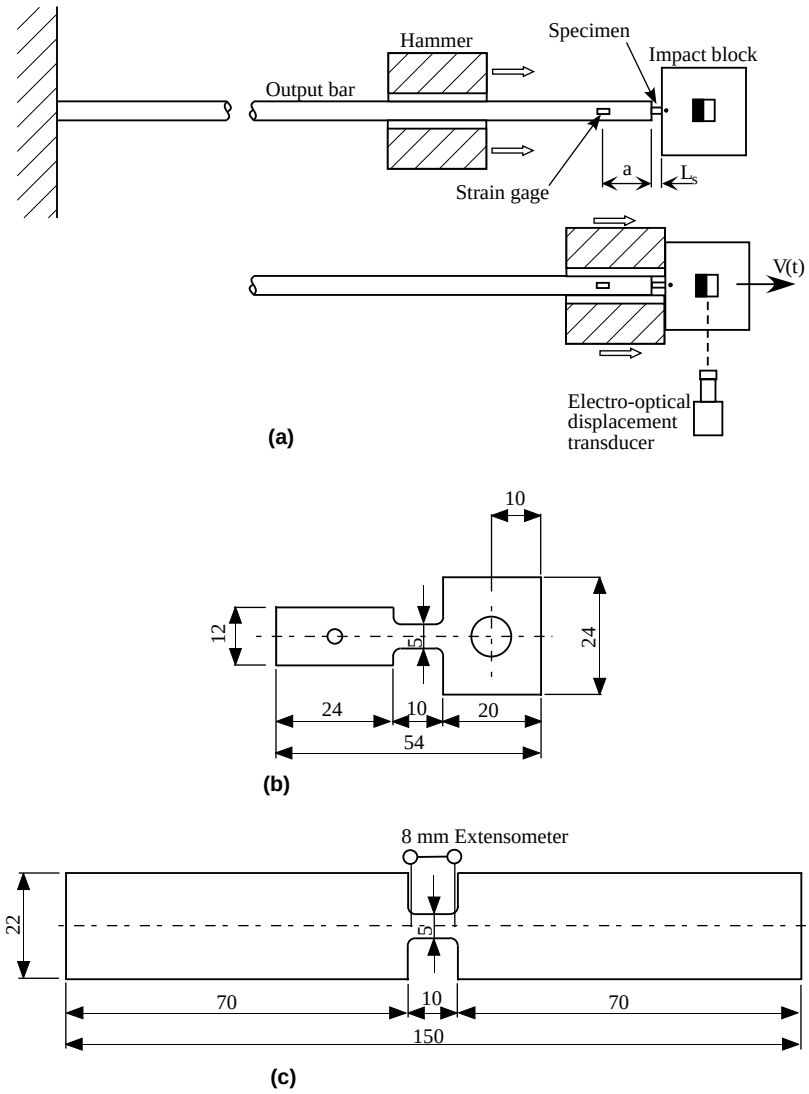

Fig. 2. Testing method and specimens: (a) schematic diagram of the one bar method, (b) specimen for high strain rate tensile tests with the one bar method, (c) specimen for quasi-static tensile tests with an Instron-type machine.

curves for the strain rates of 250/s and 750/s are very different from those for the strain rates of 0.001/s, 0.1/s and 1/s. The initial peak of stress (to say a distinct upper yield limit) develops in the cases of the strain rates of 250/s and 750/s. This stress peak is a real material response, not a pseudo-peak caused by vibration effects, as mentioned before. The drop of the tensile load, which prompts a diffuse neck development and the subsequent fracture, occurs much earlier at the strain rates of 250/s and 750/s than at the lower strain rates. These results are in agreement with those reported in Uenishi and Teodosiu (2003). It is seen from Fig. 4 that the breakage occurred after the sufficient development of diffuse neck. Hence, a ductile fracture is said to occur even at a high strain rate of 750/s, although the term "high-velocity brittleness" was defined and used to represent the phenomenon of the reduction in elongation at high strain rates (Kawata et al., 1985).

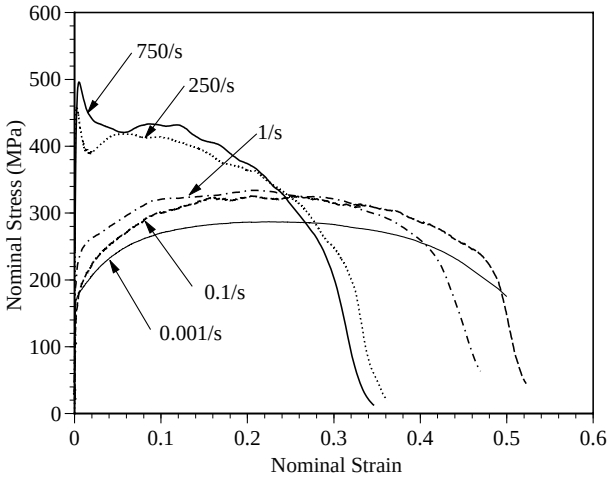

Fig. 3. Curves of nominal stress versus nominal strain at different strain rates (experiments).

Fig. 4. Specimens after tensile tests at nominal strain rates of 750/s (left) and of 0.001/s (right).

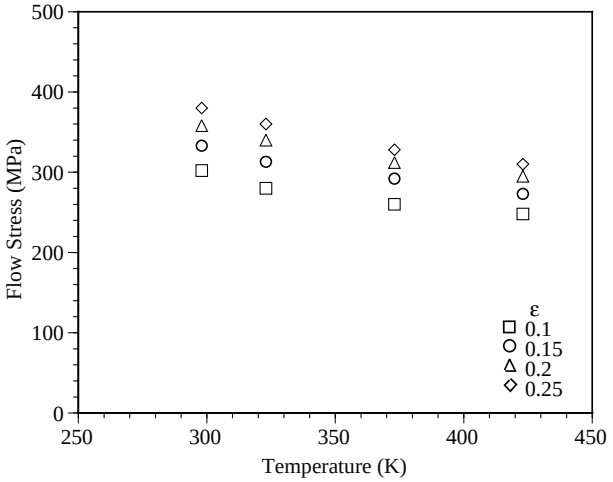

Fig. 5. Thermal softening behavior: relationships between flow stress and temperature.

Table 1
Experimentally measured Lankford's r-values

Tensile direction relative to RD	r-Value
0°	2.22
45°	1.85
90°	2.77

In addition to the above experiments, we conducted other sets of tensile tests, using conventional dumbbell-shaped specimens, in order to measure the temperature dependence of flow stress and Lankford's r-values (the ratio of width to thickness plastic strain). Fig. 5 shows the results for the temperature dependence of flow stress (true stress) at various levels of uniaxial true strain (the tensile axis coincided with RD for all the cases). These tensile tests were carried at a nominal strain rate of 0.002/s. Table 1 shows the r-values at a 15% plastic strain for three tensile directions, i.e. 0°, 45° and 90° relative to RD. The r-values will be used to evaluate the plastic anisotropy of the sheet.

3. Constitutive modeling

3.1. Preliminary: physically-based considerations

The slip rate $\dot{\gamma}$ on any active slip system in a crystal is given by Orowan's equation,

$$\dot{\gamma} = b\rho_{\mathrm{m}}\bar{v}, \tag{3}$$

where b is the magnitude of the Burgers vector, ρ_{m} is the density of the mobile dislocations, and $\bar{v}$ is the average velocity of the mobile dislocations in the direction of the slip vector for the considered slip system.

For thermally activated dislocation motion, the average velocity $\bar{v}$ of moving dislocations is modeled by an Arrhenius type of equation

$$\bar{v} = \omega_0 \ell \exp\left(-\frac{\Delta G}{kT}\right), \tag{4}$$

where ℓ is the average effective barrier spacing, ω_0 is the attempt frequency of the dislocation segment, k is the Boltzmann constant, T is the absolute temperature, and ΔG is the activation energy that a dislocation must use through its thermal activation in order to overcome its short-range barrier. It follows from Eqs. (3) and (4) that

$$\dot{\gamma} = \dot{\gamma}_{\mathrm{R}} \exp\left(-\frac{\Delta G}{kT}\right) \tag{5}$$

with

$$\dot{\gamma}_{\mathrm{R}} \equiv b\rho_{\mathrm{m}}\omega_0\ell. \tag{6}$$

Several formulations for ΔG have been suggested, using a concept of additive decomposition of athermal and thermal activation parts of stress (e.g. Kocks et al., 1975). Alternatively, several more phenomenological models for $\dot{\gamma}$ have been proposed, such as models by Johnston (1962) and by Hahn (1962). In both the approaches, $\dot{\gamma}$ can be written in a general form

$$\dot{\gamma} = \dot{\gamma}_{\mathrm{R}} \cdot \Psi(\tau, \gamma, T), \tag{7}$$

where Ψ is a function of the resolved shear stress τ acting on the slip system, the amount of slip γ and the temperature T.

Usually, the factor $\dot{\gamma}_R = b\rho_m\omega_0\ell$ defined in Eq. (6) is assumed to be constant, because (i) ω_0 is constant, (ii) ℓ is constant ($= b$) for the Peierls barrier in most b.c.c. metals, and (iii) it is generally considered that the mobile dislocation density ρ_m is *approximately* constant during steady plastic straining. Therefore, if we suppose a variation in $\dot{\gamma}_R$, it must reflect directly the change in ρ_m, i.e. we question the above assumption (iii). It has been known that the yield-point phenomenon of iron and related b.c.c. metals is well reproduced when $\dot{\gamma}_R$ is assumed to increase with plastic strain γ (Johnston and Gilman, 1959; Johnston, 1962; Hahn, 1962; Yoshida, 2000).

3.2. Macroscopic constitutive modeling

In this study, we intend to perform numerical computations using a macroscopically formulated constitutive model, not crystal plasticity. Approaches to macroscopic modeling of the viscoplastic behavior of metals at a high strain rate are roughly divided into two groups. One is approaches based on Eq. (5), in which ΔG is assumed as a function of thermally activated component of the flow stress at a macroscopic scale (e.g. Kocks et al., 1975; Zerilli and Armstrong, 1987; Nemat-Nasser and Guo, 2003). The other is more phenomenological approaches apart from Eq. (5) (e.g. Johnson and Cook, 1983; Khan and Liang, 1999).

In both the approaches, a general form for viscoplastic models is written as

$$\dot{\Phi} = \dot{\varepsilon}_R \cdot \Psi(\bar{\sigma}, \varepsilon^p, T) \tag{8}$$

similar to Eq. (7), where $\dot{\Phi}$ is a strain rate in one-dimensional theories or an overstress function in three-dimensional theories, $\dot{\varepsilon}_R$ is a reference strain rate, $\bar{\sigma}$ is an equivalent stress, and ε^p is an equivalent plastic strain. We have to give appropriate formulations for Ψ and $\dot{\varepsilon}_R$.

Firstly, here we adopt the following phenomenological expression for Ψ:

$$\Psi(\bar{\sigma}, \varepsilon^p, T) = \exp\left(\frac{\bar{\sigma} - g(\varepsilon^p)\cdot\Omega(T)}{D\cdot\Omega(T)}\right), \tag{9}$$

where $g(\varepsilon^p)$ is a strain hardening function, D is a viscosity parameter with dimension of stress, which, in general, may vary with ε^p, and $\Omega(T)$ is a nondimensional thermal softening function. Use of Eq. (9) in Eq. (8) gives

$$\bar{\sigma} = \left[g(\varepsilon^p) + D\ln\left(\frac{\dot{\Phi}}{\dot{\varepsilon}_R}\right)\right]\Omega(T). \tag{10}$$

When we regard $g(\varepsilon^p)$ and D respectively as $g(\varepsilon^p) = C_1 + C_2\varepsilon^{pn}$ and $D = C_3\cdot\ g(\varepsilon^p)$ with C_1, C_2, and C_3 being material constants, the model of Eq. (10) is identified with Johnson–Cook (JC-) (Johnson and Cook, 1983) model that had much success in various engineering applications. In case of the original JC-model, the derivative of $g(\varepsilon^p)$ with respect to ε^p becomes infinite at $\varepsilon^p \to 0$. This is a rather severe restriction for reproducing experimental stress–strain curves. For this reason, in our model, $g(\varepsilon^p)$ is taken to be the following equation

$$g(\varepsilon^p) = \sigma_{y0}\left(1 + \frac{\varepsilon^p}{\varepsilon_0}\right)^n, \tag{11}$$

where σ_{y0} is a reference stress, ε_0 and n are material parameters. In case of JC-model, the hardening rate $d\bar{\sigma}/d\varepsilon^p$ at a certain strain will increase when the strain rate increases, because the viscosity parameter D increases depending on the increase in $g(\varepsilon^p)$, as is schematically illustrated in Fig. 6(a). According to Liang

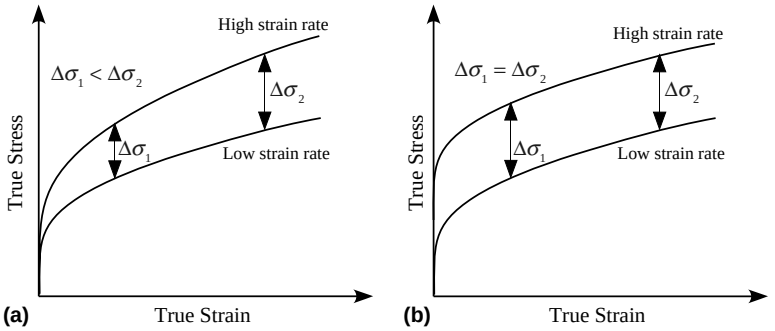

Fig. 6. Schematic illustrations of true stress–true strain curves at different strain rates: (a) Johnson–Cook-like model with the viscosity parameter D that increases with ε^{p}; (b) a model with a constant D.

and Khan (1999), the direct dependence of D on $g(\varepsilon^{\mathrm{p}})$ yields appropriate predictions for the behavior of copper and nickel. Our preliminary investigation suggested, however, that this dependence yields poor predictions for the behavior of IF steel, whereas an assumption that D is constant gives a good correlation with experimental results. The schematic illustration with the assumption of constant D is given in Fig. 6(b).

The thermal softening function is taken to be

$$\Omega(T) = 1 - \left(\frac{T - T_{\mathrm{R}}}{T_{\mathrm{M}} - T_{\mathrm{R}}}\right)^{p}, \tag{12}$$

where T_{R} is a reference temperature, T_{M} is the melting temperature of the material, and p is a material constant. Since the material response under room temperature is considered here, T_{R} is chosen to be room temperature.

Next, we will formulate the reference strain rate $\dot{\varepsilon}_{\mathrm{R}}$. The $\dot{\varepsilon}_{\mathrm{R}}$ in Eq. (8) corresponds to $\dot{\gamma}_{\mathrm{R}}$ in the slip rate model (Eq. (7)). In most applications, $\dot{\varepsilon}_{\mathrm{R}}$ has been assumed to be constant. Contrary to these approaches, we consider here a time dependence of $\dot{\varepsilon}_{\mathrm{R}}$. That is, it is assumed that the mobile dislocation density ρ_{m} increases with passing of time under a certain stress condition, because the initial mobile dislocation density in IF steel is normally not sufficient to generate plastic flow at steady state. Nesterova et al. (2001) reported based on a TEM observation that the matrix grains in an undeformed IF steel occurred practically dislocation free. If we consider plastic straining only at quasi-static strain rates, the rise time of the dislocation density can be negligible compared to observed time. As far as high strain rate deformation is concerned, this assumption should be challenged. Thus, time dependence of the mobile dislocation density is considered here. The natural time, t, is not appropriate as a measure of internal time in the material, in principle, because the change in temperature and the change in strain rate are equivalent from a viewpoint of the thermal activation concept. As an internal time parameter, the following nondimensionalized $\bar{t}$ is introduced:

$$\bar{t} = t \cdot \bar{\nu}(T). \tag{13}$$

Here, the coefficient $\bar{\nu}(T)$ is defined by

$$\bar{\nu}(T) = \bar{\nu}_{\mathrm{R}} \exp\left[-A\left(\frac{1}{T} - \frac{1}{T_{\mathrm{R}}}\right)\right], \tag{14}$$

where A is a material parameter having the dimension of temperature, $\bar{\nu}_{\mathrm{R}}$ is a parameter having the dimension of (natural time)$^{-1}$. Eq. (14) is derived, assuming that a change in the average frequency of thermal motion of atoms is proportional to $\exp(-A/T)$. According to Eq. (13) with Eq. (14), the natural time at any temperature T is normalized to the time scale at T_{R}.

An *effective* internal time parameter $\bar{t}^{\text{eff}}$ for "plastic" straining is defined by

$$\bar{t}^{\text{eff}} = \langle \bar{t}^{\text{p}} - \bar{t}_{\text{lag}} \rangle \tag{15}$$

with

$$\bar{t}^{\text{p}} = t^{\text{p}} \cdot \bar{v}(T), \quad t^{\text{p}} = \int \mathrm{d}t \quad \text{for } \bar{\sigma} > \sigma_{\text{FR}}(T), \tag{16a, b}$$

$$\bar{t}_{\text{lag}} = t^{\text{R}}_{\text{lag}} \cdot \bar{v}_{\text{R}}. \tag{17}$$

Here, $\langle\ \rangle$ are the Macauley brackets, t^{p} is the natural passing time for *plastic* straining, $\sigma_{\text{FR}}(T)$ is a stress value beyond which the Frank–Read mechanism becomes *macroscopically* active, and $t^{\text{R}}_{\text{lag}}$ is the initial *lag* time of material response observed at T_{R}, which corresponds to a finite time period for initial generation of the mobile dislocations.

Using the effective internal time parameter, $\bar{t}^{\text{eff}}$, introduced above, the time dependence of $\dot{\varepsilon}_{\text{R}}$ is formulated as

$$\dot{\varepsilon}_{\text{R}} = f_1(\bar{t}^{\text{eff}}) \cdot f_2(\varepsilon^{\text{p}}), \tag{18}$$

where the function $f_1(\bar{t}^{\text{eff}})$ having dimension of (natural time)$^{-1}$ portrays phenomenologically the influence of increase in ρ_{m} with $\bar{t}^{\text{eff}}$, while the dimensionless function $f_2(\varepsilon^{\text{p}})$ models the increase in ρ_{m} with increasing plastic deformation. When $f_1(\bar{t}^{\text{eff}})$ is assumed to be constant, the framework of the model reduces to that of the yield-point models (Johnston and Gilman, 1959; Johnston, 1962; Hahn, 1962; Yoshida, 2000). Meanwhile, Eq. (18) can describe the phenomenon that ρ_{m} increases with $\bar{t}^{\text{eff}}$, if $f_1(\bar{t}^{\text{eff}})$ is properly formulated. In this study, the latter case is considered, assuming that $f_2 = 1$ throughout the deformation.

In the present study, the function $f_1(\bar{t}^{\text{eff}})$ is taken to be

$$f_1(\bar{t}^{\text{eff}}) = \dot{\varepsilon}_{\text{r0}} + (\dot{\varepsilon}_{\text{ra}} - \dot{\varepsilon}_{\text{r0}})[1 - \exp(-\bar{t}^{\text{eff}})], \tag{19}$$

where $\dot{\varepsilon}_{\text{r0}}$ and $\dot{\varepsilon}_{\text{ra}}$ ($\dot{\varepsilon}_{\text{r0}} < \dot{\varepsilon}_{\text{ra}}$) with dimension of (natural time)$^{-1}$ are the initial and asymptotic values of $f_1(\bar{t}^{\text{eff}})$, respectively. Eq. (19) models, in a macroscopic manner, the phenomenon that the initially low mobile dislocation density increases with passing time under the stress condition shown in Eq. (16b). This is a natural consideration for IF steels, as is explained before. In this paper, Eq. (19), as a first choice among numerous possibilities, is applied to predictions of the material behavior under a rather narrow range of temperature. Therefore, we assume that $\bar{v}(T) \approx \bar{v}(T_{\text{R}}) = \bar{v}_{\text{R}}$ for simplicity in the present application. Then, the definition of $\bar{t}^{\text{eff}}$ reduces to

$$\bar{t}^{\text{eff}} = \langle t^{\text{p}} - t^{\text{R}}_{\text{lag}} \rangle \bar{v}_{\text{R}}. \tag{20}$$

Under this simplification, we need not specify the value of the additional material constant A.

3.3. Three-dimensional description of the constitutive model

Since we consider a rolled sheet of IF steel, effects of plastic anisotropy due to crystallographic texture are not negligible. The equivalent stress $\bar{\sigma}$ is represented by Hill's quadratic function (Hill, 1948),

$$\bar{\sigma} = \sqrt{\frac{3}{2(F+G+H)}}[F(\hat{\sigma}_{22} - \hat{\sigma}_{33})^2 + G(\hat{\sigma}_{33} - \hat{\sigma}_{11})^2 + H(\hat{\sigma}_{11} - \hat{\sigma}_{22})^2 + 2L\hat{\sigma}^2_{23} + 2M\hat{\sigma}^2_{31} + 2N\hat{\sigma}^2_{12}]^{1/2}, \tag{21}$$

where F, G, H, L, M and N are anisotropic coefficients assumed to be constant for simplicity, and $\hat{\sigma}_{ij}$ are the components of Cauchy stress tensor $\boldsymbol{\sigma}$ in reference to the orthotropic axes $\hat{x}_i$. The rolling direction, RD, the

transverse direction, TD, and the normal direction, ND, are chosen to coincide initially with the axes $\hat{x}_1$, $\hat{x}_2$ and $\hat{x}_3$, respectively. The orthonormal base (unit) vectors corresponding to $\hat{x}_i$ are denoted by $\mathbf{n}_i$, then the stress components on this triad are calculated by $\hat{\sigma}_{ij} = \mathbf{n}_i \cdot \boldsymbol{\sigma} \cdot \mathbf{n}_j$. When $3F = 3G = 3H = L = M = N$, Eq. (21) reduces to the von Mises equivalent stress.

The σ_{y0} in Eq. (11) and D in Eq. (10) are determined by

$$\sigma_{y0} = \sqrt{\frac{3(G+H)}{2(F+G+H)}}\sigma_0, \tag{22}$$

$$D = \sqrt{\frac{3(G+H)}{2(F+G+H)}}D_0, \tag{23}$$

where σ_0 and D_0 are a reference stress and a viscosity parameter determined through uniaxial tension tests in the $\hat{x}_1$-direction (RD). The coefficient with F, G and H in front of σ_0 and D_0 in Eqs. (22) and (23) have been introduced so that Eq. (10) reduces to

$$\hat{\sigma}_{11} = \left[\sigma_0\left(1+\frac{\varepsilon^{\mathrm{p}}}{\varepsilon_0}\right)^n + D_0 \ln\left(\frac{\dot{\Phi}}{\dot{\varepsilon}_{\mathrm{R}}}\right)\right]\Omega(T) \tag{24}$$

for the uniaxial tension in the $\hat{x}_1$-direction. In the isotropic case, $\sigma_{y0} = \sigma_0$ and $D = D_0$.

We choose the current configuration of deformed solid as the reference state. In the following description of the three-dimensional model, a fixed rectangular Cartesian coordinate system is used. The spatial velocity gradient is represented by $l_{ij} = \partial v_i/\partial x_j$, where v_i is the velocity of the material particle and x_j is its current position. The l_{ij} is decomposed into the rate of deformation d_{ij} and the continuum spin w_{ij} as

$$l_{ij} = d_{ij} + w_{ij}, \tag{25}$$

$$d_{ij} = \frac{1}{2}(l_{ij} + l_{ji}), \tag{26}$$

$$w_{ij} = \frac{1}{2}(l_{ij} - l_{ji}). \tag{27}$$

Throughout the present paper, we assume that elastic deformation is much smaller than plastic deformation. The rate of deformation d_{ij} is decomposed into elastic and plastic parts as

$$d_{ij} = d^{\mathrm{e}}_{ij} + d^{\mathrm{p}}_{ij}, \tag{28}$$

where superscripts e and p stand for 'elastic' and 'plastic'. We assume a linear elastic response for the elastic part d^{e}_{ij}:

$$\overset{\nabla}{\sigma}_{ij} = C_{ijkl}d^{\mathrm{e}}_{kl} = C_{ijkl}(d_{kl} - d^{\mathrm{p}}_{kl}), \tag{29}$$

$$\overset{\nabla}{\sigma}_{ij} \equiv \dot{\sigma}_{ij} - w_{ik}\sigma_{kj} + \sigma_{ik}w_{kj}, \tag{30}$$

where the superposed dot denotes the material time derivative, C_{ijkl} is a fourth order elastic moduli, which is, in this paper, assumed to be determined by Young's modulus E and Poisson's ratio ν, and the superposed ∇ denotes the Jaumann rate with respect to the continuum spin w_{ij}.

The plastic rate of deformation is given by a viscoplastic flow rule,

$$d^{\mathrm{p}}_{ij} = \dot{\Phi}N^{\mathrm{p}}_{ij}, \tag{31}$$

where the tensor N^{p}_{ij} defines the 'direction' of d^{p}_{ij}, and $\dot{\Phi}$ is given by Eq. (8) with Eqs. (9), (18), (19). In this paper, an associated flow rule is adopted, i.e. $N^{\mathrm{p}}_{ij} \equiv \partial\bar{\sigma}/\partial\sigma_{ij}$. The equivalent plastic strain ε^{p} is defined by $\varepsilon^{\mathrm{p}} = \int\sqrt{(2/3)d^{\mathrm{p}}_{ij}d^{\mathrm{p}}_{ij}}\mathrm{d}t$.

Assuming the adiabatic condition for high strain rate tensile tests (higher than 100/s), the heating of the material due to the dissipated plastic work can be derived from

$$\dot{T} = \frac{\alpha_{\mathrm{h}}}{\rho c_{\mathrm{p}}} \sigma_{ij} d^{\mathrm{p}}_{ij}, \tag{32}$$

where ρ is the mass density, c_{p} is the specific heat, α_{h} is the heat conversion ratio taken equal to unity in the case of adiabatic heating for high strain rate tensile tests (faster than 100/s). For low strain rate tensile tests (slower than 1/s), we assume the isothermal condition, i.e. $\dot{T}$ is set to be zero.

During deformation, it is assumed that the orthonormal vectors $\mathbf{n}_i$ attached to the anisotropic axes rotate according to the continuum spin tensor $\mathbf{w}$, i.e. $\dot{\mathbf{n}}_i = \mathbf{w} \cdot \mathbf{n}_i$. This is a rather simple approximation compared to the previous studies (Kuroda, 1997, 1999; Kuroda and Tvergaard, 2000, 2001a) in which the plastic spin concept was introduced. In the present problem, the three orthotropic axes of the material initially coincide respectively with the thickness, width and tension directions of the specimen, and the rotation of the axes will not be so large. Therefore, it is believed that the above simple assumption is sufficient for the present tensile problem.

4. Computations of tensile tests and comparison with experimental results

4.1. Computational procedure and problem formulation

In the computational procedure, the constitutive equation, Eq. (29) with Eq. (31), is rewritten by use of a rate-tangent modulus method (Peirce et al., 1984), in order to perform stable numerical calculations. Then, the constitutive equation is implemented into a finite element method. As mentioned in Section 2, the tensile tests at high strain rates were performed using the improved one bar method (Yoshida, 2001; Uenishi et al., 2003), which can extract features of the exact material response free from any apparent vibrational phenomenon that would be caused by the multiple passage of reflected longitudinal elastic waves. Corresponding to this, the finite element method employed is based on a quasi-static formulation without the inertial effect (e.g. McMeeking and Rice, 1975).

The finite element model of the tensile specimen is shown in Fig. 7. Considering symmetric conditions of the specimen, only one octant portion is modeled. Twenty node isoparametric three-dimensional elements

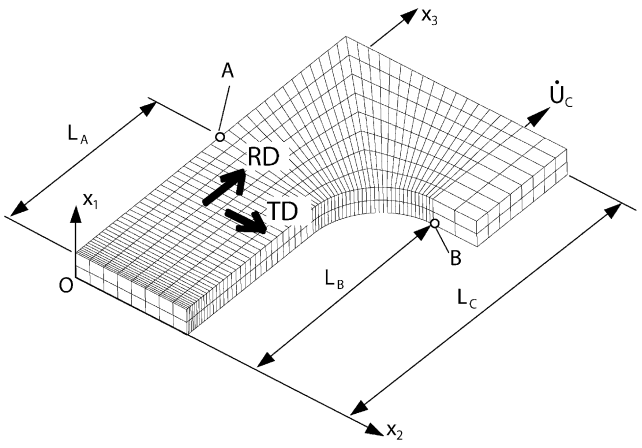

Fig. 7. Simplified finite element model of the tensile specimen.

with eight Gaussian integration points (reduced integration) are used. The model geometry is rather simplified in comparison to the whole geometry of the real specimens shown in Fig. 2. But, this model is sufficient to predict the plastic deformation behavior of the specimen, because the part outside the parallel gage region will undergo extremely small plastic deformation even after the parallel gage region is subjected to a very severe plastic deformation.

The boundary conditions of the model are

$$\begin{aligned}
&v_1 = 0 \quad \text{and} \quad \dot{q}_2 = \dot{q}_3 = 0 \quad \text{on } X_1 = 0,\\
&v_2 = 0 \quad \text{and} \quad \dot{q}_1 = \dot{q}_3 = 0 \quad \text{on } X_2 = 0,\\
&v_3 = 0 \quad \text{and} \quad \dot{q}_1 = \dot{q}_2 = 0 \quad \text{on } X_3 = 0,\\
&v_3 = \dot{U}_C \quad \text{and} \quad v_1 = v_2 = 0 \quad \text{on } X_3 = L_C,
\end{aligned}$$

where X_i denotes the position of a material particle in the initial configuration, and $\dot{q}_i$ denotes the traction rate. All the remaining surfaces are traction free. The prescribed displacement rate $\dot{U}_C$ is determined from the corresponding experimental condition. The point A corresponds to the position at which the extensometer for the low strain rate tensile tests was attached, and L_A is taken to be 4 mm, according to the length of the extensometer shown in Fig. 2(c). The length L_B is 5 mm, following the size of the specimen. The length L_C is taken to be 7.5 mm. RD is initially coincident with the tensile axis.

4.2. Computational results and comparison with experimental results

Fig. 8 shows the dependence of the flow stress on temperature and its approximation by use of Eq. (12). The data plotted in Fig. 8 are reproduced from Fig. 5, but are normalized by the flow stress at T_R (= 298 K) for each strain level. With the melting temperature approximated as $T_M \approx 1800$ K, the exponent p in Eq. (12) is determined as 0.685 by a regression analysis.

Ratios of the anisotropic coefficients F/H, G/H and N/H are determined using the r-values shown in Table 1, i.e.

$$\frac{F}{H} = \frac{1}{r_{90}}, \quad \frac{G}{H} = \frac{1}{r_0}, \quad \frac{N}{H} = \left(r_{45} + \frac{1}{2}\right)\left(\frac{1}{r_0} + \frac{1}{r_{90}}\right), \tag{33}$$

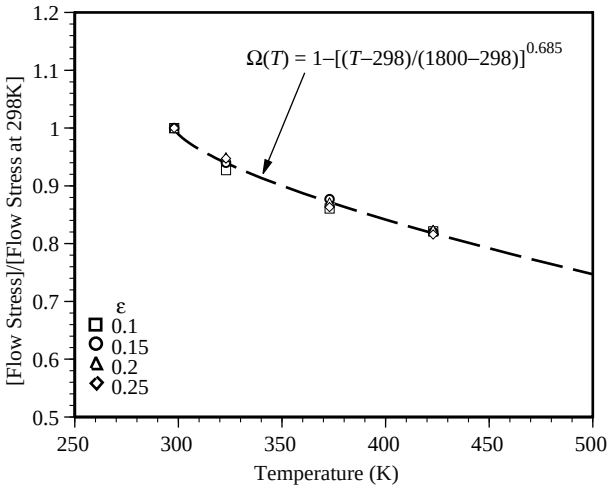

Fig. 8. Determination of the thermal softening function.

where r_0, r_{45} and r_{90} are the r-values at 0°, 45° and 90° relative to RD. The remaining two anisotropic coefficients L and M cannot be determined from the present experimental data. Here, we assume that $L = M = 3H$. It is believed that the assumption does not much affect the results because the shear stress components $\hat{\sigma}_{23}$ and $\hat{\sigma}_{31}$ remain small compared to the other stress components.

The strain hardening parameters, σ_0, ε_0 and n, and the viscosity parameter, D_0, are determined using the experimental data for the low strain rate tension tests. The values of the material parameters for $\dot{\varepsilon}_R$ (i.e. $\dot{\varepsilon}_{r0}$, $\dot{\varepsilon}_{ra}$, t^R_{lag} and $\bar{\nu}_R$) are determined with reference to the results for the high strain rate tension tests. It is difficult to estimate these parameter values by completely independent experiments, because the measurement of continuous variation in the mobile dislocation density during high strain rate deformation is a formidable task. Nevertheless, the model of $\dot{\varepsilon}_R$ in Eqs. (18)–(20) with only the four parameters is sufficiently simple for representing the complicated viscoplastic behavior of IF steel. Table 2 summarizes the values of all the constants for numerical computations.

Computed curves of nominal stress versus nominal strain are depicted in Fig. 9(a) and (b), together with the corresponding experimental curves reproduced from Fig. 3. Fig. 9(a) shows the results for the nominal strain rates of 250/s and 750/s. The nominal strain in the computations is calculated as U_B/L_B, where U_B is the displacement of the point B (see Fig. 7) in the x_3-direction. The adiabatic condition has been assumed. As is seen from Fig. 9(a), good correlation between the experimental results and the computational results is obtained, except for the final stage of the deformation, i.e. the computations do not predict the sudden drop of the nominal stress at the final stage. The initial stress peak has been reproduced in the computations.

Fig. 9(b) shows the results for the nominal strain rates of 0.001/s, 0.1/s and 1/s. In these computations, the nominal strain is calculated as U_A/L_A, where U_A is the displacement of the point A (see Fig. 7) in the x_3-direction. It is seen that the model somewhat overestimates the ductility of the specimens. This may be partly attributed to the assumption of the constant D (or D_0) for the whole range of strain rate considered here, which might have been too simple. As is known, a small variation in the viscosity much affects the strain localization behavior (e.g. Kuroda and Tvergaard, 2001b). Although there is such a quantitative discrepancy between the experimental and the computational results at low strain rates, the fundamental material responses observed in the experiments are predicted by the proposed model.

Table 2
Values of the constants for the IF-steel

Constants	Values	Constants	Values
E [GPa]	200	T_M [K]	1800
ν	0.3	p	0.685
σ_0 [MPa]	180	ρ [kg/m^3]	7.87×10^3
ε_0	0.00675	c_p [J/kg/K]	461
n	0.22	α_h	1.0
D_0 [MPa]	10.8	F	0.361
t^R_{lag} [s]	1.0×10^{-5}	G	0.450
$\dot{\varepsilon}_{r0}$ [/s]	1.0×10^{-9}	H	1.0
$\dot{\varepsilon}_{ra}$ [/s]	0.1	L	3.0
$\bar{\nu}_R$ [/s]	50	M	3.0
$\sigma_{FR}(T_R)$ [MPa]	10[a]	N	1.91
T_R [K]	298		

[a] The critical resolved shear stress to activate the Frank–Read mechanism is given by $\tau_{FR} = \mu b/\bar{d}$, where μ is the shear elastic modulus (≈80 GPa), b is the magnitude of Burgers vector (= 0.25 nm), and $\bar{d}$ is the average distant between pinning points for dislocations, which was estimated by a SEM observation as 1–10 μm. Using these values, τ_{FR} is estimated as 2–20 MPa, and here σ_{FR} is assumed to be 10 MPa. But, it has been confirmed that the value of σ_{FR} does not much affect the computational results.

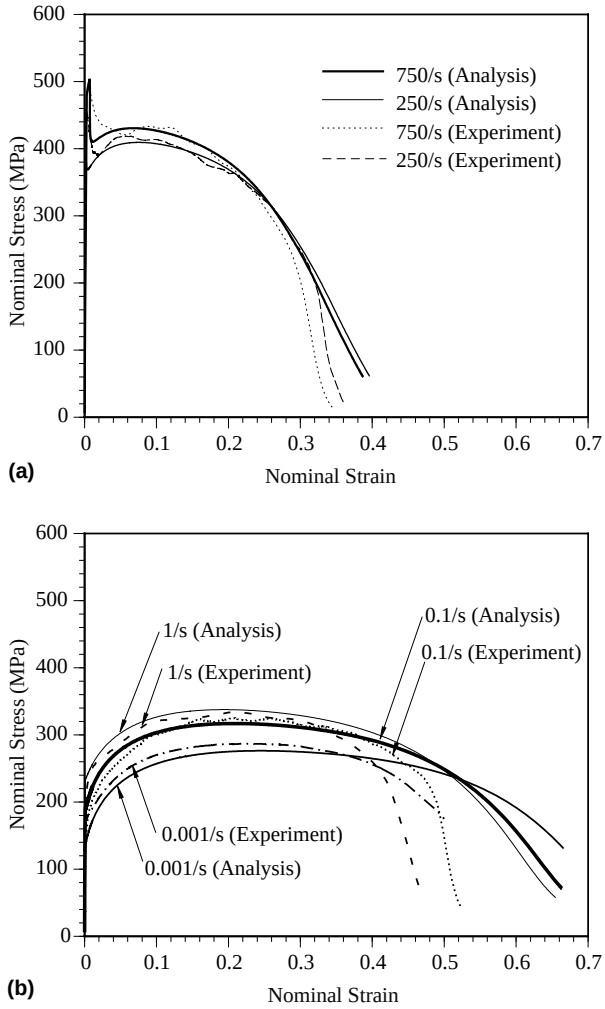

Fig. 9. Comparison of computed nominal stress–nominal strain curves to experimental results (a) for strain rates of 250/s and 750/s (the adiabatic condition is assumed in the computations), and (b) for strain rates of 0.001/s, 0.1/s and 1/s (the isothermal condition is assumed).

Figs. 10 and 11 show deformed meshes and contours of the equivalent plastic strain ε^{p} at three stages of elongation for nominal strain rates of 750/s and of 0.1/s, respectively. Fig. 10(a) shows the deformed state right after the occurrence of the initial peak of nominal stress. The overall deformation and the distribution of the plastic strain are almost identical to those shown in Fig. 11(a) that depicts the result for 0.1/s at almost the same amount of elongation. This means that the occurrence of the initial peak of nominal stress has no significant effect on the progress of deformation. The experimentally observed deformation behavior including the diffuse neck formation (Fig. 4) has been well reproduced by the computation. The computations have taken into account the material anisotropy through the *r*-values. The IF steel used here has rather high *r*-values whose average is more than two (see Table 1). In the case of a material with high *r*-values, the reduction of width is more dominant than the reduction of thickness. Within the diffuse neck region, the neck in the width direction develops largely rather than thinning, as is seen in Fig. 10(d). It has

been confirmed that a more significant thinning and a less reduction of the width are predicted when isotropy is assumed, although their depiction is omitted here. In the present constitutive model, any effect of material damage and breakage is not accounted for. At the deformation stage corresponding to Fig. 10(c) and (d) (at a nominal strain of 0.320), the drop of the tensile load in the experiment is very steep, as is seen in Fig. 9(a). The breakage might have already started in the real specimen at this stage.

In the computations shown in Fig. 9(a) and Fig. 10 for strain rates of 250/s and 750/s, the adiabatic heating has been assumed. Fig. 12 exhibits the effect of the thermal softening on the predicted results through a comparison of the cases of the adiabatic and isothermal conditions. It is clearly seen that the thermal softening yields a lower tensile load and less ductility. But, it is clear that the fundamental characteristic of the

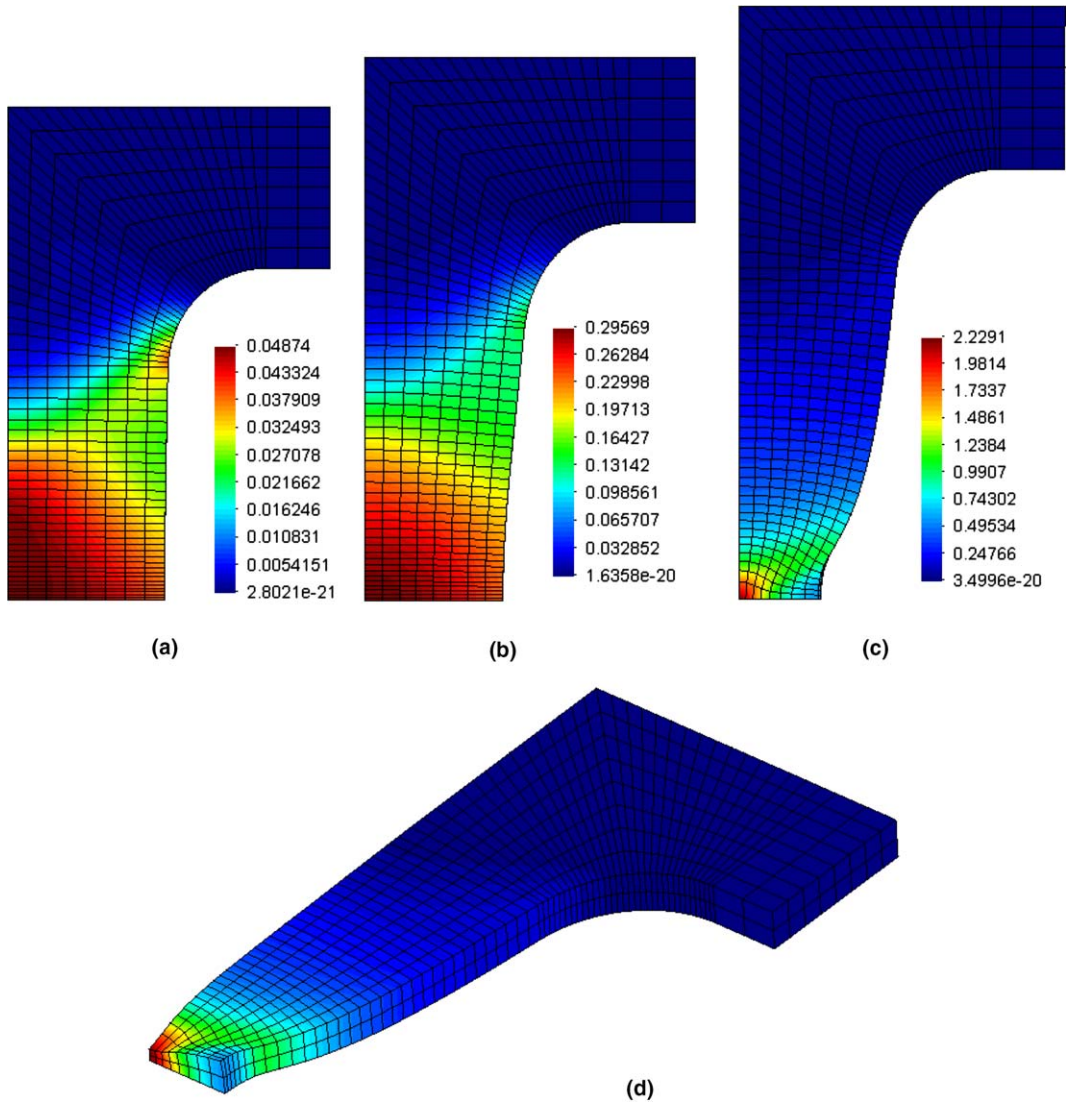

Fig. 10. Deformed finite element meshes and contours of equivalent plastic strain at nominal strains of (a) 0.028, (b) 0.148 and (c) 0.320 for a nominal strain rate of 750/s. (d) shows a different view of (c).

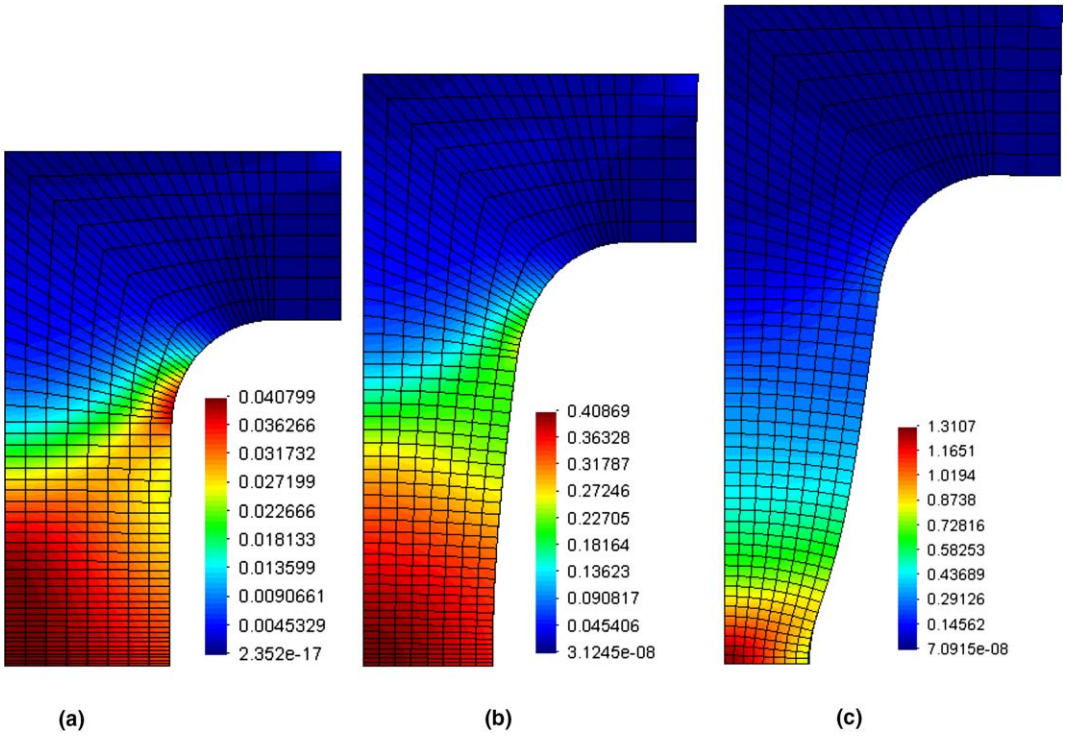

Fig. 11. Deformed finite element meshes and contours of equivalent plastic strain at nominal strains of (a) 0.032, (b) 0.309 and (c) 0.533 for a nominal strain rate of 0.1/s.

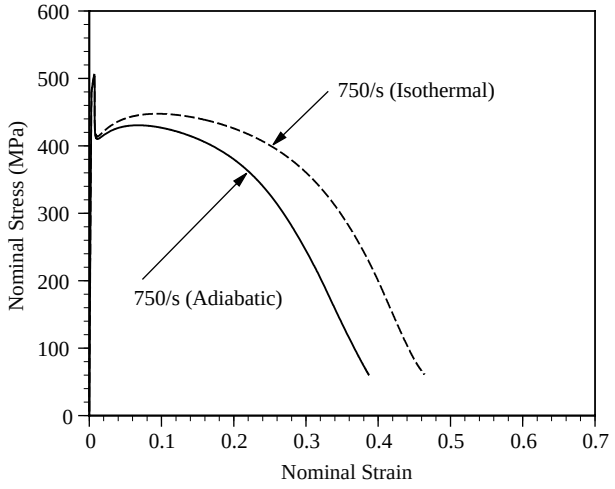

Fig. 12. Effect of thermal softening on computed nominal stress–nominal strain curves for a strain rate of 750/s.

mechanical response has been predicted without the heating and softening effects. This means that the typical stress–strain response of IF steel at a high strain rate has been captured mainly by the present time-dependent model of $\dot{\varepsilon}_R$.

5. True stress–strain relations

In our experimental investigation with the thin IF steel sheet, *true stress–true strain relations* could not be extracted directly from the experimental results, because the significant neck development occurs in the tensile tests, as already shown, unlike in the compression tests using Hopkinson-bar technique with a thick cylindrical specimen. The proposed model with the material parameter values given in Table 2 could reproduce rather well the nominal stress–nominal strain relations and the deformation behavior including the neck formation, especially at high strain rates. It is considered that the true stress–true strain curves can reasonably be reproduced by performing simulations of a uniaxial *uniform* tension with the same set of the material parameter values.

Fig. 13 shows computed true stress–true strain curves at various nominal strain rates, which were obtained using a single finite element (assuming homogeneous deformation). Fig. 14 shows curves of

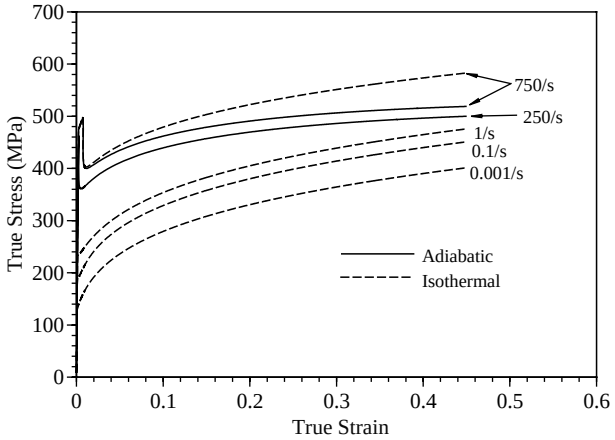

Fig. 13. Computed uniaxial true stress–true strain relations at various nominal strain rates.

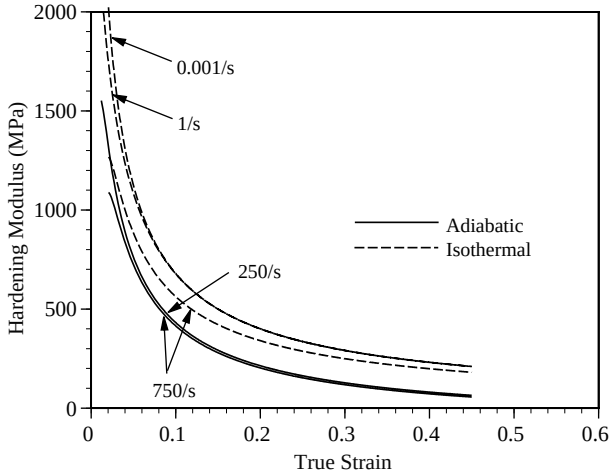

Fig. 14. Hardening modulus (slope of uniaxial true stress–true strain curve) calculated from the curves shown in Fig. 13.

hardening modulus (slope of true stress–true strain curve) versus true strain, which are calculated from the curves shown in Fig. 13. (The moduli corresponding to the initial stress peak at high strain rates have not been depicted.) Smaller hardening modulus is observed at the higher strain rates even in the case of isothermal condition. The small $\dot{\varepsilon}_R$ at an initial stage of deformation, which physically corresponds to a small initial amount of ρ_m, causes the significant rise in stress at the early stage of high strain rate tension, even if the initial stress peak is left out of consideration. This stress rise at the early stage induces a subsequent smaller hardening modulus. It is clear that the smaller hardening modulus yields an earlier formation of diffuse neck (e.g. Swift, 1952). Then, the less ductility is observed for a high strain rate tensile test.

6. Concluding remarks

The final breakage of the IF steel sheet specimen at a high strain rate occurs after the diffuse neck has developed, as is seen in Fig. 4. Thus, the fracture of IF steel at a high strain rate is fairly said to be a *ductile fracture*. However, the ductility of IF steel is significantly reduced at a high strain rate. The reduction of ductility is caused by an earlier development of the diffuse neck. The occurrence of the diffuse neck is governed by the amount of instantaneous hardening modulus, which is strain rate dependent. A smaller hardening modulus yields an earlier development of diffuse neck. In the proposed constitutive model, the smaller hardening modulus at a high strain rate, which is observed in the real material, is reproduced thanks to the time-dependent relation for the reference strain rate $\dot{\varepsilon}_R$, Eq. (18) with Eq. (19). The small amount of $\dot{\varepsilon}_R$ at an initial stage of deformation causes a significant rise in the flow stress at an early stage, and then $\dot{\varepsilon}_R$ increases with passing time under a certain stress condition. The time-dependent $\dot{\varepsilon}_R$ models macroscopically the phenomenon that an initially low mobile dislocation density increases significantly with continuous loading. This is a natural consideration for IF steel that has properties similar to pure irons. It is shown in Figs. 9–11 that the present constitutive model has a sufficient capability to reproduce the mechanical response of IF steel over a wide range of strain rates.

The present model, which is described in Section 3.2, has been formulated macroscopically. One may consider a direct use of a *physically-based* thermal activation model (e.g. Kocks et al., 1975) for $\Psi(\bar{\sigma}, \varepsilon^p, T)$ instead of Eq. (9). This is worth pursuing. In this case, a more physical model for $\dot{\varepsilon}_R$ in which realistic value and variation of ρ_m are considered should be formulated.

In conclusion, a new macroscopic viscoplastic model has been proposed, taking into account the effect of the change in the mobile dislocation density. The proposed model has a sufficient capability to reproduce the strongly strain rate sensitive material response of IF steel.

Acknowledgements

The authors gratefully acknowledge valuable scientific discussion with Drs. M. Takahashi and Y. Kuriyama (Nippon Steel Corporation).

References

Hahn, G.T., 1962. A model for yielding with special reference to the yield-point phenomena of iron and related bcc metals. Acta Metallurgica 10, 727–738.

Hill, R., 1948. Theory of the yielding and plastic flow of anisotropic metals. Proceedings of Royal Society of London A 193, 281–297.

Itabashi, M., 2003. High velocity tensile test for thin plate specimen with one bar method. JSME International Journal A 46, 316–321.

Johnson, G.R., Cook, W.H., 1983. A constitutive model and data for metals subjected to large strains, high strain rates and high temperatures. In: Proceedings of the Seventh International Symposium on Ballistic. The Hague, The Netherlands, pp. 541–547.

Johnston, W.G., 1962. Yield points and delay times in single crystals. Journal of Applied Physics 33, 2716–2731.
Johnston, W.G., Gilman, J.J., 1959. Dislocation velocities, dislocation densities and plastic flow in lithium fluoride crystals. Journal of Applied Physics 30, 129–144.
Kawata, K., Hashimoto, S., Kurokawa, K., Kanayama, N., 1979. A new testing method for the characterization of materials in high velocity tension. In: Harding, J. (Ed.), Mechanical Properties at High Rates of Strain 1979. Institute of Physics, Bristol and London, pp. 71–80.
Kawata, K., Hashimoto, S., Takeda, N., Sekino, S., 1985. On high-velocity brittleness and ductility of dual-phase steel and some hybrid fiber reinforced plastics. In: Recent Advances in Composites in the United States and Japan. ASTM Special Technical Publications, Philadelphia, pp. 700–711.
Khan, A.S., Liang, R., 1999. Behaviors of three BCC metals over a wide range of strain rates and temperatures: experiments and modeling. International Journal of Plasticity 15, 1089–1109.
Kocks, U.F., Argon, A.S., Ashby, M.F., 1975. Thermodynamics and kinetics of slip. Progress in Material Science 19, 1–271.
Kuroda, M., 1997. Interpretation of the behavior of metals under large plastic shear deformations: a macroscopic approach. International Journal of Plasticity 13, 359–383.
Kuroda, M., 1999. Interpretation of the behavior of metals under large plastic shear deformations: comparison of macroscopic predictions to physically based predictions. International Journal of Plasticity 15, 1217–1236.
Kuroda, M., Tvergaard, V., 2000. Forming limit diagrams for anisotropic metal sheets with different yield criteria. International Journal of Solids and Structures 37, 5037–5059.
Kuroda, M., Tvergaard, V., 2001a. Plastic spin associated with a non-normality theory of plasticity. European Journal of Mechanics A/Solids 20, 893–905.
Kuroda, M., Tvergaard, V., 2001b. Shear band development predicted by a non-normality theory of plasticity and comparison to crystal plasticity predictions. International Journal of Solids and Structures 38, 8945–8960.
Liang, R., Khan, A.S., 1999. A critical review of experimental results and constitutive models for bcc and fcc metals over a wide range of strain rates and temperatures. International Journal of Plasticity 15, 963–980.
McMeeking, R.M., Rice, J.R., 1975. Finite-element formulations for problems of large elastic–plastic deformation. International Journal of Solids and Structures 11, 601–616.
Nemat-Nasser, S., Guo, W.-G., 2003. Thermomechanical response of DH-36 structural steel over a wide range of strain rates and temperatures. Mechanics of Materials 35, 1023–1047.
Nesterova, E.V., Bacroix, B., Teodociu, C., 2001. Microstructure and texture evolution under strain-path changes in low-carbon interstitial-free steel. Metallurgical and Materials Transactions A 32A, 2527–2538.
Peirce, D., Shih, C.F., Needleman, A., 1984. A tangent modulus method for rate dependent solids. Computers and Structures 18, 875–887.
Swift, H.W., 1952. Plastic instability under plane stress. Journal of the Mechanics and Physics of Solids 1, 1–18.
Uenishi, A., Teodosiu, C., 2003. Solid solution softening at high strain rates in Si- and/or Mn-added interstitial free steels. Acta Materialia 51, 4437–4446.
Uenishi, A., Yoshida, H., Kuriyama, Y., Takahashi, M., 2003. Material characterization at high strain rates for an optimization of car body structure. Nippon Steel Technical Report 378, pp. 21–24.
Yoshida, F., 2000. A constitutive model of cyclic plasticity. International Journal of Plasticity 16, 359–380.
Yoshida, H., 2001. Exact indentification of strain rate dependency of steel properties by one bar method. In: Proceedings of the 52nd Japanese Joint Conference for Technology of Plasticity, Fukui, pp. 175–176.
Zerilli, F.J., Armstrong, R.W., 1987. Dislocation-mechanics-based constitutive relations for material dynamics calculations. Journal of Applied Physics 61, 1816–1825.